BIO-INSPIRED BUCKLING JOINTS IMPROVE POST-COLLISION STABILITY IN FLAPPING WINGS: A STRUCTURAL DYNAMICS PERSPECTIVE

by

Jenna Rose McNally

A thesis submitted in partial fulfillment
of the requirements for the degree

of

Master of Science

in

Engineering

MONTANA STATE UNIVERSITY
Bozeman, Montana

Dec 2025

DEDICATION

I dedicate this thesis to my friends and family. To my grandparents, Jerry and JoLouise, for their unwavering interest and support in my education, and to my parents, Steve and Faith, whose love and guidance made this achievement possible. I certainly would not be here without you.

ACKNOWLEDGEMENTS

First, I would like to thank my advisor, Dr. Mark Jankauski, for his invaluable guidance throughout this project. His mentorship has helped me grow as a researcher and writer. I would also like to thank my committee members, Dr. Perrin Schiebel and Dr. Lewis Cox and faculty in the MIE department for their wisdom and support. Finally, a special thank you to my friends at MSU and in the Bio-inspired Dynamics lab for their encouragement, collaboration, and camaraderie.

Funding Acknowledgment: This research was supported by the National Science Foundation under award no. CMMI-1942810 to M.J. and DGE-2439625 to J.M. Any opinions, findings, and conclusions or recommendations expressed in this material are those of the author(s) and do not necessarily reflect the views of the National Science Foundation.

TABLE OF CONTENTS

1. INTRODUCTION 1

Wing damage and insect strategies for collision avoidance 1
Passive mechanisms in insect wings for collision management 2
Active and Passive Control strategies in FWMAVs 5
Research Gap 7

2. BIO-INSPIRED BUCKLING JOINTS IMPROVE POST-COLLISION STABILITY IN FLAPPING WINGS: A STRUCTURAL DYNAMICS PERSPECTIVE 8

Contribution of Authors and Co-Authors 8
Manuscript Information 9
Introduction 10
Methods 12
Experimental Design 12
Torque-Angular Displacement Test 14
Dynamic Disturbance Test 15
Results 17
Torque-Angular Displacement Study 17
Dynamic Disturbance Tests 18
Discussion 21
Buckling Test Beam Exhibits Hysteresis 22
Test Beam Improved Stability in Dynamic Disturbance Experiments 23
Implications in Robotics 24
Acknowledgments 25
Data Availability 26

3. CONCLUSION 27

Concluding Remarks 27
Key Findings 27
Supplemental Findings 29
Future Directions 29

REFERENCES CITED 32

LIST OF TABLES

Table Page

1. Table 1 Design dimensions for the test beam and control beam. All dimensions reported in millimeters. Variable definitions illustrated in Fig.6 13

LIST OF FIGURES

Figure Page

1. Figure 1 A rhinoceros beetle hind wing in unfolded (A) and folded (b) configurations from [1]. 3
2. Figure 2 An unsplinted (A) and splinted (B) yellowjacket wing during collision from [2]. (C) Image of a yellowjacket wing costal break from [3]. 4
3. Figure 3 Locust hindleg extended (A) and buckled (B) with blue florescence indicating the presence of resilin. [4] 4
4. Figure 4 Robobee wing (A) with integrated hinging joint (B) from [5]. 6
5. Figure 5 Tailless flapping-wing robot (A) from [1] with integrated folding wing (B) 7
6. Figure 6 (A) The test beam (orange) and control beam (white) used for all experiments. (B) Schematic of the experimental setup used for torque-angular displacement and dynamic disturbance tests with defined dimensions for test beam parameters. (C) Image of the experimental setup as used in the lab. 12
7. Figure 7 (A) Torque-angular displacement data for 15 regular loading cycles from which hysteresis area was calculated. The control beam (purple) and the test (blue) have lightly colored loading regimes and darkly colored unloading regimes. (B) Representative time-series torque data of three loading cycles at 1 Hz loading frequency for both the control beam (dark blue) and test beam (light blue). 18
8. Figure 8 (A to D) Kinematic data from the disturbance trials (light purple) at the range extremes in comparison to an undisturbed trial (dark purple). Control beam at the lowest torque input setting (A) and highest (C). Test beam at the lowest torque input setting (B) and highest (D). (E) ISE values for the control beam (dark blue) and test beam (light blue) at the 9 different input torque values. 19

LIST OF FIGURES – CONTINUED

Figure Page

9. Figure 9 (A and B) Representative time series data for 5 trials of the control beam (A) and the test beam (B) at the lowest torque input setting. (C) Angular impulse measurements for the control (dark blue) and the test (light blue) beams at the 9 different input torque settings. 20

10. Figure 10 (A and B) Representative torque-angular displacement data for 5 trials of the control beam (A) and the test beam (B) at the lowest torque input setting. (C) Angular work measurements for the control (dark blue) and the test (light blue) beams at the 9 different input torque settings. 21

ABSTRACT

Flapping wing micro air vehicles (FWMAVs) have received significant attention in recent years for their size, maneuverability, and potential use in dangerous or congested environments. However, FWMAVs are susceptible to destabilization following in-flight wing collisions, which are inevitable. In recent work, bio-inspired buckling mechanisms have been introduced into FWMAV wings to improve collision robustness by passively mitigating destabilizing effects. However, the physical mechanisms by which these joints influence vehicle stability remain poorly understood. To better understand the role of buckling joints in stability, we designed a test beam comprised of two flexible segments interconnected by a buckling joint. The test beam was subjected to a series of quasi-static torque-displacement and dynamic disturbance tests. Results of the test beam were compared against a homogeneous control beam. In quasi-static torque–displacement tests, the test beam dissipated 3 times more energy compared to the control beam as indicated by hysteresis loops. In dynamic disturbance tests, the test beam exhibited reduced path disturbance as described by the Integral of Squared Error (ISE), which quantifies the cumulative deviation of a signal from a reference trajectory over time. Specifically, the test beam reduced average ISE by over 90% from the control averages for 6 out of 9 input conditions tested. The improved trajectory recovery in the test beam results from lower angular impulse and work imparted by the disturbance. Overall, angular work done by the disturbance was 3 times higher for the control beam than the test beam and the maximal average impulse imparted by the disturbance was approximately 5 times higher for the control beam than the test beam at the same input setting. This study advances the understanding of how bio-inspired buckling joints can improve FWMAV stability following collisions.

INTRODUCTION

Flapping wings enable efficient and robust flight in natural fliers. Insects and birds that utilize flapping wing flight are highly maneuverable [6] [7], fly at incredibly low Reynolds numbers [8] and have the ability to hover [9]. Natural fliers have become an excellent source of bio-inspiration as the demand for smaller aerial robots increases [10, 11] and many researchers have adopted their flapping-wing design [12–17] leading to the emergence of a new class of aerial vehicles known as flapping-wing micro air vehicles (FWMAVs). These drones show promise for applications in congested or hazardous environments, such as search and rescue, environmental monitoring, and military surveillance. However, FWMAVs still have significant limitations, including damage mitigation and stability enhancement post collision. Here, we examine some of the biomechanical strategies insects use to withstand and recover from collisions and how they might be applied to solve key design challenges related to collision robustness in FWMAVs.

Wing damage and insect strategies for collision avoidance

Insects navigate congested vegetation during flight while foraging, mate seeking, or avoiding predators, often resulting in collisions. Collisions are the most likely cause of wing wear, cumulative damage that insect wings undergo over an individual's lifespan [18], and can be costly. In observational studies of both honeybees and bumblebees, wing wear was correlated to increased mortality [19, 20] and in controlled experiments with artificially induced wing damage, wear was found to affect flight performance [21] of bumblebees and foraging behavior [19] in honeybees. To mitigate these costs, insects employ behavioral and sensory strategies for collision avoidance. Recent studies provide evidence that bumblebees use gap perception relative to their wingspan, adjusting their flight path to avoid narrow openings that could otherwise result in wing strikes [22] and that honeybees use optic flow sensing to maintain safe distances from nearby surfaces while navigating through cluttered environments [23]. Another study using fruit flies, showed how they may employ brightness-based sensing, where variations in light intensity guide their flight decisions and help them avoid obstacles [24]. Although there is evidence that sensing and flight control play a large role in collision management in insects, collisions are still inevitable. For instance, bumblebees have been observed to strike vegetation roughly once per second during foraging [18]. So, in addition to obstruction sensing and collision avoidance, many insects exhibit embodied collision robustness; structural anatomical features in their wings and bodies that allow them to withstand impacts and continue flying. These passive biomechanical adaptations complement active control strategies, ensuring that insects can maintain stability and functionality even when collisions are frequent.

Passive mechanisms in insect wings for collision management

Insect wings are compliant structures and their flexibility has been shown to enhance lift generation [25, 26]. While flexibility provides this benefit, wings must also resist excessive bending due to aerodynamic flight forces; so insect wings strike a balance between stiffness and compliance [27]. Insect wings have longitudinal veins for stiffening the wing, with flexible membranes between [25–28]. Additionally, insect wing stiffness is highly anisotropic, with spanwise flexural stiffness measured to be 10–100 times greater than chordwise stiffness, a difference attributed primarily to the structural reinforcement of the leading-edge vein [29]. However, during a collision, stiff wings can transmit counter-torques from the disturbance, destabilizing flight and imposing elevated stresses on the wing that increase the risk of structural damage [3]. Some insects employ collapsible hinge-like joints that allow for both stiff and compliant states of the wing, reducing damage and improving stability following a collision.

For example, rhinoceros beetles possess hindwings with collapsible, origami-like folds that act as shock absorbers during impact [1]. At rest, the hindwings are folded beneath the elytra and are rapidly unfolded through flapping forces within two wing beats when they take flight. Extended and folded configurations of a beetle hindwing are shown in Figure 1 [1]. These wing folds also collapse during flight after contact with an obstacle, preventing the beetle from tumbling, and deploy back to their extended position within a wing stroke. In an in-flight wing collision study, insects' attitudes were less perturbed in instances where the wings folded up compared to instances where the wings did not fold. Yaw angle and yaw rate had the most significant improvement from the folding.

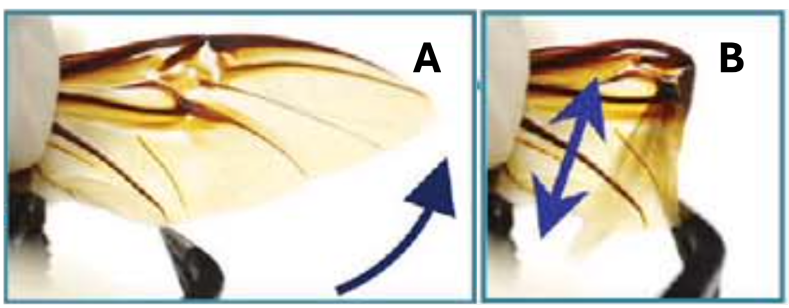

Figure 1: A rhinoceros beetle hind wing in unfolded (A) and folded (b) configurations from [1].

The costal break, a joint along the leading edge vein in certain Hymenopteran wings, remains in tact under normal flight loads but becomes compliant once a critical angle is exceeded. Experiments have shown that this feature plays a direct role in mitigating wing damage during collisions. When the costal break was splinted in yellowjackets, their wings experienced significantly greater area loss and more rapid area loss under repeated impacts [2]. The experimental setup from the controlled collision studies is shown in Figure 2.A and 2.B. Additionally, in a wing impact modeling study, representing the costal break as a torsional spring, with a decreased stiffness after some critical angle, significantly enhanced post-impact stability by reducing reaction moments [3].

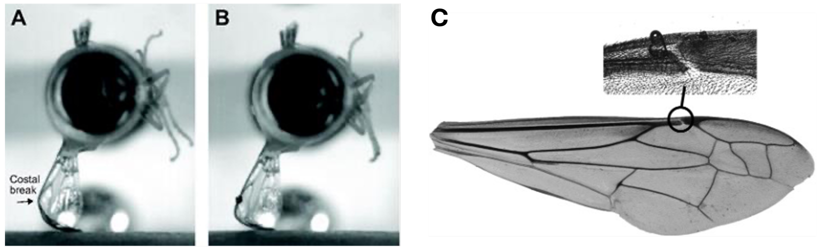

Figure 2: An unsplinted (A) and splinted (B) yellowjacket wing during collision from [2]. (C) Image of a yellowjacket wing costal break from [3].

A similar buckling mechanism has been identified in locust hindlegs [4]. The hindleg buckling is shown in Figure 3, where blue florescence indicates the presence of resilin. Although this insect mechanism is unrelated to flight collision robustness, it has a similar function for errors in jumping and kicking. When the joint buckles, it absorbs excess kinetic energy from a jump or kick that does not make contact. In work loops from repeated buckling, the joint was shown to store up to half (870 µJ) of the energy that would be expended during a kick (1700 µJ).

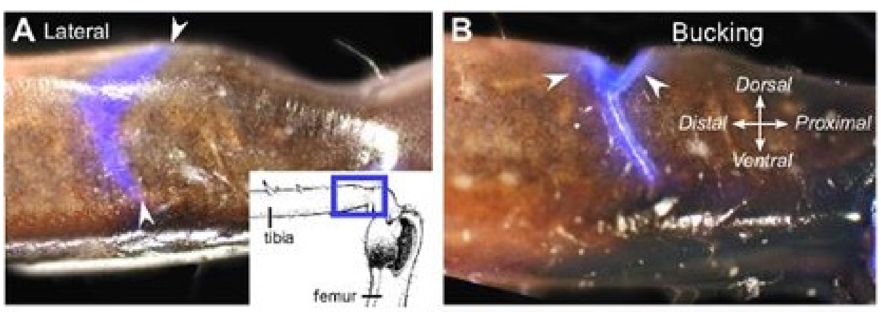

Figure 3: Locust hindleg extended (A) and buckled (B) with blue florescence indicating the presence of resilin. [4]

Insects rely on a combination of both sensory functions and embodied intelligence to navigate dense environments without catastrophic damage or losing control. Collapsible folding wings in beetles, costal breaks in yellowjackets, and buckling hindlegs in locusts all function to reduce transmitted loads and dissipate energy passively, while sensory systems help detect and avoid collisions altogether. Given their success in insects, researchers are interested in integrating both sensing and passive mechanisms inspired by insects into FWMAVs and other robotic systems to improve collision detection and passive recovery.

Active and Passive Control strategies in FWMAVs

Some recent work aims to improve collision sensing and active recovery strategies for flapping-wing micro aerial vehicles (FWMAVs). A vision-based obstacle avoidance algorithm integrated into the CNUX Mini FWMAV, utilizes appearance variation cues and optical flow-based techniques to detect obstacles. In validation tests the robot had a 90.2% success rate in evading obstacles [30]. Another study employs wing-strain-based flight control using the aerodynamic forces exerted on a FWMAV's wings to deduce attitude and airflow data [31]. Similarly, a hummingbird inspired drone used actuator loading to sense disturbances and demonstrated the ability to terrain follow through a narrow path [32].

In addition to sensing and control integration, researchers have investigated various passive mechanical designs to increase the collision tolerance of FWMAVs and rotary MAVs. The Rotorigami [33], is a halo-like protective system that decouples a MAV from collision induced moments. Additionally, it has an origami structure that absorbs impact energy and reduces peak impact forces resulting from collisions. Another FWMAV uses a cylindrical tumbler inspired damping mechanism that improves altitude stabilization time by 20 times compared to previous work without dampers [34]. The mechanism centers aerodynamic pressure above the vehicle's center of mass and generates vortex-distribution-induced restoring moments that stabilize the vehicle along the vertical axis during motion. The vehicle was able to withstand consecutive disturbances in collision and wind gust tests. Another FWMAV employs compliance within its actuators to enhance collision robustness [35]. Piezoelectric-powered MAVs are prone to cracking under large loads and strains resulting from wingtip collisions or aggressive maneuvers [36]. In contrast, this dielectric elastomer actuator (DEA)-powered FWMAV has demonstrated the ability to perform aggressive maneuvers, such as somersaults, and to recover successfully from collisions without damage [35].

Several FWMAV designs have passive buckling features inspired by insect joints to improve collision robustness and stability. A costal break-inspired collapsible wing hinge reduced post-collision attitude disruption in a RoboBee [5]. The hinge was designed to replicate the strain weakening behavior of the costal break in yellow jackets in torque-deflection tests, and effectively reduced yaw position and rate disruption in free flight tests. Yaw rates were reduced by approximately 40 % compared to a non-buckling wing.

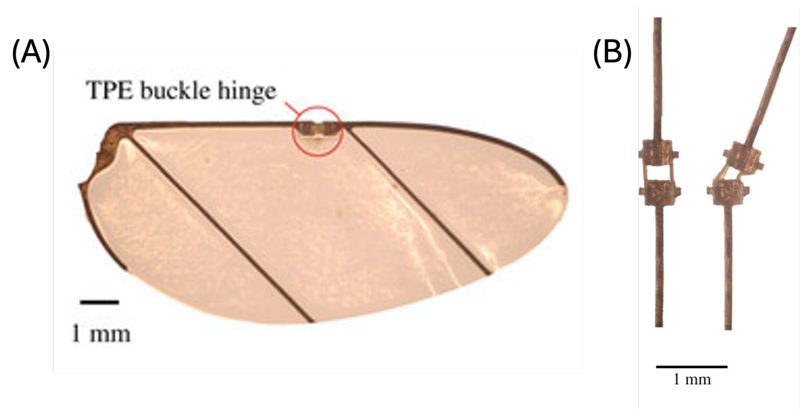

Figure 4: Robobee wing (A) with integrated hinging joint (B) from [5].

Similarly, a dual-stiffness frame, also inspired by the costal break, improved crash resilience in a quadcopter [37]. While at a different scale, the dual stiffness frame operates under the same principle as the costal break, stiff during flight, and compliant upon collision. This design enabled the drone to maintain efficient flight under normal conditions, while also surviving impacts that could cause catastrophic failure in a rigid frame. Another flying robot equipped with a folding wing joint modeled after beetle hindwings was designed to mimic the torque–deflection behavior of the beetle's MJ joint [1]. In free flight experiments, the robot was able to navigate gaps smaller than its wingspan and survived collisions without tumbling. The folding-wing FWMAV experienced reduced attitude disruption during collisions compared to configurations without the folding function.

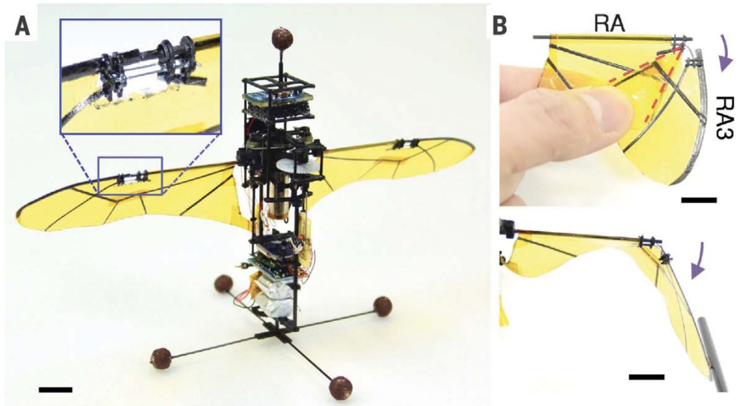

Figure 5: Tailless flapping-wing robot (A) from [1] with integrated folding wing (B)

Research Gap

Prior studies have demonstrated how embodied mechanical intelligence in insects can inspire robotic buckling mechanisms that improve stability after in-flight disturbances. However, these stability results were largely evaluated from system attitude tracking in free-flight studies. In effect, there is evidence that buckling compliance improves stability, but the underlying mechanics describing the hinge buckling remain unresolved. Without this mechanistic understanding, it is difficult to generalize design principles across different scales, materials, or wing architectures. What is missing is a reductionist approach that isolates how the buckling joint behaves structurally under collision loading conditions. To fill this gap, we designed controlled experiments to compare a bio-inspired buckling jointed beam to a homogeneous control beam in collision loading. We subject both beams to a quasi-static loading test to identify material dissipation behavior, and dynamic disturbance tests from which we measured kinematic path following, angular impulse, and work done by the disturbance. From these measurements, we can better understand the mechanisms responsible for stability improvements for a buckle joint design.

BIO-INSPIRED BUCKLING JOINTS IMPROVE POST-COLLISION STABILITY IN FLAPPING WINGS: A STRUCTURAL DYNAMICS PERSPECTIVE

Contribution of Authors and Co-Authors

Manuscript in Chapter 2

Author: Jenna McNally

Contributions: data curation, investigation, methodology, formal analysis, software, data visualization, original draft, writing-editing and reviewing.

Co-Author: Mark Jankauski

Contributions: conceptualization, funding acquisition, project administration, resources, supervision, methodology, formal analysis, original draft, writing-reviewing, and editing.

Manuscript Information

Jenna McNally & Mark Jankauski

Bioinspiration & Biomimetics

Status of Manuscript:
____ Prepared for submission to a peer-reviewed journal
__X__ Officially submitted to a peer-reviewed journal
____ Accepted by a peer-reviewed journal
____ Published in a peer-reviewed journal

IOP Publishing
Submitted: 10/08/25

Introduction

Flapping-Wing Micro Air Vehicles (FWMAVs) are small scale aerial robots inspired by natural fliers like insects and birds [10, 11]. Their compact design and potential for high maneuverability make them well suited for environments that are challenging for traditional aerial vehicles, such as dense urban areas or disaster zones [12–17, 34]. Despite their promise for applications in search and rescue, environmental monitoring, and surveillance, current FWMAVs face significant limitations. Among these is their ability to cope with in-flight collisions. To overcome this challenge, recent work to improve FWMAVs has focused on understanding the mechanisms insects employ to mitigate the implications of collision.

Collisions or disturbances during flight can compromise critical wing functions in insects. Wings serve as the control surfaces that provide the lift necessary to fly and play a role in various sensory functions as well. For instance, moth wings have been found to possess gyroscopic sensing capabilities, allowing them to detect rotational movements and maintain stability during flight through posture control [38]. Additionally, dragonflies have been found to use bristles on their wings for flow sensing, improving their flight control in changing flow conditions [39]. Given these important aerodynamic and sensory roles, damage from collisions can be especially costly. Wing wear, the cumulative degradation of wings over time, has been shown to increase mortality in both honeybees [19] and bumble bees [20]. In controlled experiments with artificially induced wing damage, wear affected flight performance [21] and foraging behavior [19]. However, insects must navigate complex and congested environments where collisions are inevitable. Bumblebees, for example, have been observed to strike vegetation roughly once per second during foraging [18]. Further, wing collisions can impart counter-torques that destabilize flight by altering angular momentum, and elevate stresses on the wing that increase wear [3].

Some insects have collapsible hinge-like joints that allow for both stiff and compliant states of the wing to improve stability and mitigate damage associated with collisions [1–3, 5]. For example, rhinoceros beetles possess collapsible origami-like hindwings that fold up during wing tip impact, resulting in less perturbed body kinematics compared to when the wings do not fold [1]. The costal break, a joint along the leading edge vein in certain Hymenopteran wings, remains stiff under normal flight loads but has strain weakening behavior at larger wing deflection angles [5]. Experiments have shown that when the costal break is splinted in yellow jackets, wings experience greater area loss under repeated impacts [2]. Numerical models suggest the costal break may enhance post-impact stability by reducing reaction moments as well [3].

Given their benefits in insects, engineers have begun implementing similar buckling structures into flying robots. For example, a collapsible wing hinge was found to decrease post collision yaw rates in an insect-scale FWMAV [5]. A quadcopter drone with an integrated dual stiffness frame inspired by insect wings survived 50 high speed collisions with no permanent damage [37]. An FWMAV with a joint inspired by beetle hindwings was able to negotiate gaps smaller than its wingspan, while decreasing yaw angle and rate disruption from a wing tip collision in comparison to the drone without the folding mechanism [1].

Though prior studies have demonstrated that insect-inspired buckling mechanisms can improve stability after disturbances in free-flying FWMAVs, the underlying mechanics of the buckling joint remain understudied. To better understand the mechanics of buckling joints, we designed experiments comparing the static and dynamic behavior of a bio-inspired buckling beam with that of a homogeneous control beam. Specifically, we performed quasi-static torque-angular displacement tests to describe energy dissipation behavior and controlled dynamic disturbance tests to evaluate trajectory disturbance, impact, and work done by an external disturbance.

Methods

We developed experiments to better understand how buckling may improve stability in flapping wing insects and insect-inspired FWMAVs. First, we developed two structures: a test beam, comprised of two segments separated by flexible parallel plates that buckle at large angles, and a homogeneous control beam. These two beams are intended to behave identically in the linear regime, which allows us to better isolate the contributions of non-linear buckling in the test beam. We first performed torque-angular displacement tests on both beams to quantify their linear stiffness and hysteresis behavior. Next, we applied a dynamic disturbance to both beams and evaluated several stability metrics, such as the angular impulse imparted by an external obstacle.

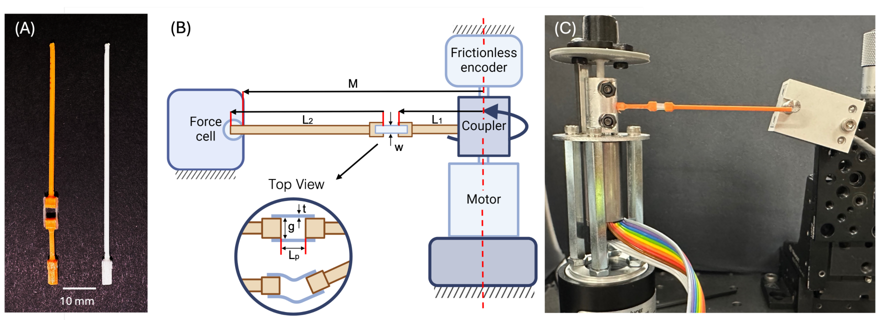

Figure 6: (A) The test beam (orange) and control beam (white) used for all experiments. (B) Schematic of the experimental setup used for torque-angular displacement and dynamic disturbance tests with defined dimensions for test beam parameters. (C) Image of the experimental setup as used in the lab.

Experimental Design

We 3D printed both test and control beam segments using a MakerBot Method X 3D printer and MakerBot Tough filament (MakerBot Industries, New York City, NY, USA), which has properties similar to ABS. For the test beam, the two segments were joined with two thin rubber plates via super glue. The plates were cut from an abrasion-resistant polyurethane rubber sheet with shore durometer 85A. The buckling joint geometry was

Table 1: Design dimensions for the test beam and control beam. All dimensions reported in millimeters. Variable definitions illustrated in Fig.6.

Variable	Description	Test Beam	Control Beam
L_1	Pre-joint beam length	20	–
L_2	Post-joint beam length	51	–
w	Plate spring width	1.7	–
g	Gap between plate springs	3.2	–
t	Plate spring thickness	0.3	–
M	Moment Arm	73	73
L	Total beam length	74	74
d	Beam diameter	1.5	1.3

motivated by that developed in [2]. The test and control beams and associated dimensions are shown in Fig. 6 and Tab. 1.

Next, we designed a motorized rotation stage for torque-angular displacement and dynamic disturbance tests (Fig. 6). A brushless DC motor (EC-max 283835, Maxon Precision Motors, Inc., Taunton, Massachusetts) was used to impose angular rotation at the base of the beams. We used a custom shaft coupler to join the motor shaft and beam structure, where the beam was suspended perpendicular to the axis of rotation. The angular position of the motor shaft was measured via a magnetic rotary encoder (MAE3, US digital, Vancouver, WA, USA). A load cell was mounted to a three-axis translation stage and positioned to oppose rotation at the beam's free end. A foil-based load cell was used for the torque angular displacement tests (GS0-100, Transducer techniques, Temecula, CA, USA) and a piezoelectric load cell (PCB 209C11, PCB Piezotronics, Depew, NY, USA) was used in the dynamic disturbance tests. The force measurement (with the knowledge of the moment arm) allows us to calculate the external disturbance torque. For the test beam, we oriented the buckling joint parallel to force cell contact such that the parallel plates buckled when the beam was subject to large rotation by the motor. A schematic of the buckled joint is shown in Fig. 6B.

We used a National Instruments data acquisition system (cDAQ-9174, National

Instruments, Austin, TX, USA) interfaced to LabVIEW 2020 software for data collection. Measurements were recorded at 1 kHz for the torque-angular displacement tests, and 15 kHz for the dynamic tests. We used two different digital positioning motor controllers in the study. The first controller used a position feedback mode (EPOS2 24/5 367676, Maxon Motor AG, Sachsein, Switzerland), which was suitable for controlling a sinusoidal displacement pattern in the torque-angular displacement study. The second controller used a current control mode (ESCON 36/3 EC, Maxon Motor AG, Sachsein, Switzerland) which applied a constant motor torque throughout the dynamic disturbance tests.

Torque-Angular Displacement Test

We applied cyclical loading via motor position control to characterize the linear stiffness and hysteresis behavior in the test and control beams. Hysteresis typically occurs due to energy dissipation; we expect this dissipation to be small in the control beam, where material damping is uniform throughout, and larger in the test beam, where a discrete increase in material damping occurs at the joint connecting the beam segments.

The beams were initially unloaded at 0° of angular rotation such that they were flush with the force cell. They were subsequently subjected to sinusoidal rotation with a peak-to-peak amplitude of approximately 13.5°. This angular displacement range induced total buckling behavior in the test beam while avoiding motor stall in the control beam. We performed tests at a 1 Hz loading frequency.

We measured angular displacement and external disturbance force directly in the experiment, then multiplied the force data by a moment arm to estimate torque resulting from the force cell disturbance at the beam free end. For the torque angular displacement loading tests, we applied a first-order low-pass filter with a cutoff frequency of 3 Hz to the force and angular displacement data. We analyzed 15 regular loading cycles for each test. Through peak finding on the angular displacement data, we segmented the torque response into loading and unloading phases for each of the 15 loading cycles. We then applied the trapezoidal integration method to calculate the area under each curve and quantified hysteresis as the difference between the loading and unloading areas.

Dynamic Disturbance Test

Dynamic disturbance tests were performed in current control mode, where we varied the applied motor torque. We considered two cases: an undisturbed case, where the beam was unobstructed, and a disturbed case, where the load cell stem obstructed the initial rotational motion of the beam. A solenoid valve acted as a mechanical trigger to restrict rotational motion of the beam until the motor current converged to the set value. For each beam, disturbance tests were repeated five times at each of nine motor current settings, along with one no-disturbance trial. These no-disturbance trials, which contain only kinematic data, served as a baseline trajectory against which disturbed paths were compared. A minimum motor current was selected such that the control beam would just pass through the force cell obstruction. We applied a first-order low-pass filter with a 200 Hz cutoff frequency for all data. This helped eliminate post-collision ringing in the force sensor.

We calculated the angular impulse imparted by the obstacle J by integrating the external torque over time. The angular impulse J is

$$J = \int_0^{t_c} \tau dt \tag{1}$$

where, τ is the torque as measured from the force cell and t_c is a length of time that encompasses the entire contact duration for all trials at any set input value. Because disturbance torque is zero once contact is lost, integrating beyond the contact period does not affect the impulse calculation. Representative time series disturbance torque data for one input torque magnitude can be seen in Fig. 8. The area under each curve was calculated numerically using trapezoidal method. We used the angular impulse imparted by the disturbance as a proxy for the change in system angular momentum from an external collision. We assumed that a lower angular impulse benefits stability in flapping wing insects or robotic vehicles because angular impulse influences the post-collision angular momentum of the insect body or vehicle airframe. By comparing the angular impulse in the test and control beams, we can understand how effectively the test beam reduces changes in angular momentum resulting from external disturbances.

In addition to impulse, we calculated the angular work done by the disturbance by integrating the external torque over the angular displacement via

$$W = \int_0^{\theta_c} \tau d\theta \tag{2}$$

where θ_c is the maximum angle across all trials at which the beam loses contact. Disturbance torque is zero once contact is lost, so integrating beyond this contact angle does not affect the angular work calculation. Representative torque versus angular displacement for one motor torque setting can be seen in Fig. 10. Similar to impulse, we calculated the area under each curve numerically using the trapezoidal method. We used the angular work imparted by the disturbance as a proxy for the change in system energy resulting from an external collision. We assumed that lower angular work benefits stability because it implies the external disturbance has a lesser influence on changes in system energy. Together, angular impulse and work provide a more complete picture of the system's response to a disturbance.

Finally, we used Integral Squared Error (ISE) as a metric to evaluate the beam paths against an undisturbed case. ISE is defined by

$$\text{ISE} = \int_0^{t_f} \left(\theta(t) - \theta_{\text{ref}}(t)\right)^2 \, dt \tag{3}$$

where θ is the angular displacement in a disturbed trial and θ_{ref} is the reference angular displacement measured in an undisturbed trial. ISE quantifies the total accumulated deviation from a target response over time. For each torque setting, the integration time interval was defined by the duration of the undisturbed trial spanning from 0° to 100° of angular displacement. Representative angular displacement paths over time can be seen in Fig. 8, where A and B are the lowest input torque setting and C and D are the highest input torque setting for each beam.

Results

Torque-Angular Displacement Study

Results from the torque-angular displacement experiment are shown in Fig. 7A. From about 0 - 3°, the torque-displacement curves for both control and test are nearly identical. There are no appreciable differences in loading or unloading curves in either case. This agreement in the linear regime confirms that the control and test beams exhibit comparable stiffness under small displacements, establishing a baseline for assessing differences in their nonlinear response.

From the time series data (Fig. 7B), we can see clear torque reduction as the test beam curve diverges from the linear response of the control beam. The critical buckling angle occurs at approximately 8°. We defined this angle by the location at which the torque-angular displacement curve has a slope of zero (Fig. 7A). Over 15 normal loading cycles, the test beam exhibited an average maximum torque response of 2.44 mNm, less than half that of the average maximum torque for the control beam, 5.38 mNm. Additionally, the energy dissipated per cycle was on average 98.4 μJ and 32.3 μJ for the test and control beam, respectively.

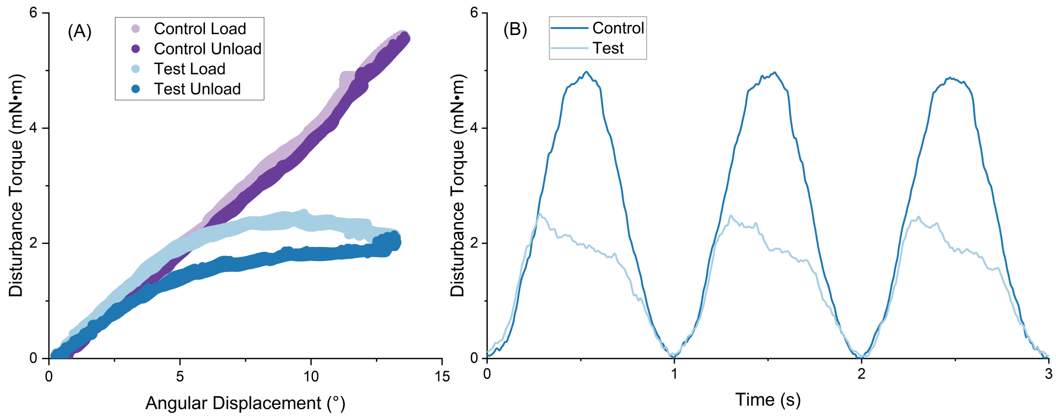

Figure 7: (A) Torque-angular displacement data for 15 regular loading cycles from which hysteresis area was calculated. The control beam (purple) and the test (blue) have lightly colored loading regimes and darkly colored unloading regimes. (B) Representative time-series torque data of three loading cycles at 1 Hz loading frequency for both the control beam (dark blue) and test beam (light blue).

Dynamic Disturbance Tests

Representative time-series angular displacement data for two of the nine input torque settings are shown in Fig. 8, with the lowest (A and B) and highest (C and D) motor input settings included to illustrate the range of tested input conditions. From these, two trends emerge that are further supported by the ISE data: (1) the test beam has better path recovery compared to the control beam, and (2) higher input torque trials exhibit better path recovery than lower input torque trials in both beams. To quantify these differences, we calculated the ISE and found that the test beam maintained consistently low values, averaging 2.39 degree^2·s at the lowest torque setting and 0.07 degree^2·s at the highest torque setting. The control beam's ISE decreased from an average of 21.19 degree^2·s at the lowest torque setting to 8.07 degree^2·s at the highest.

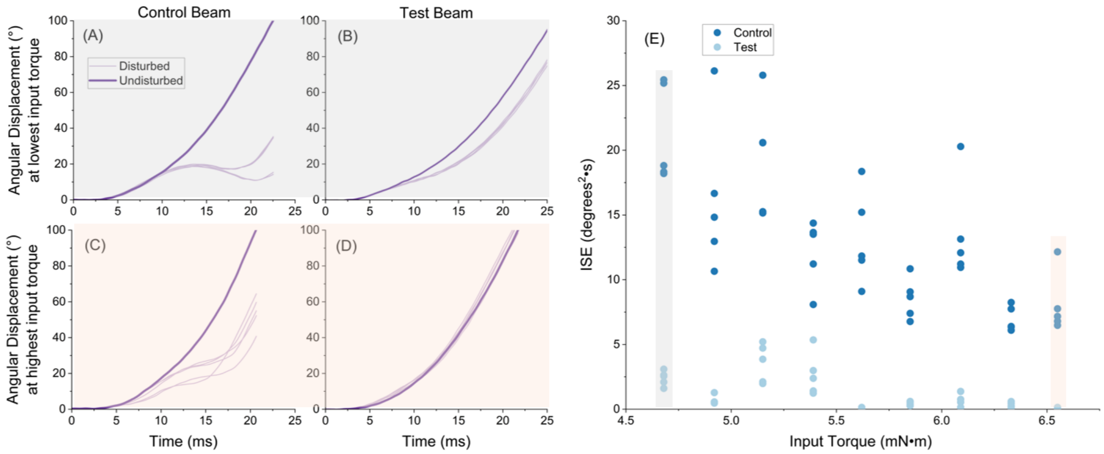

Figure 8: (A to D) Kinematic data from the disturbance trials (light purple) at the range extremes in comparison to an undisturbed trial (dark purple). Control beam at the lowest torque input setting (A) and highest (C). Test beam at the lowest torque input setting (B) and highest (D). (E) ISE values for the control beam (dark blue) and test beam (light blue) at the 9 different input torque values.

Maximum disturbance torque is reduced in the test beam compared to the control beam and can be seen in the representative time series data (Fig. 9). The peak torque occurs earlier in the test beam, whereas in the control beam it continues to increase throughout the disturbance. By integrating the time-series data, we evaluated the impulse for each trial. The test beam showed little variation in impulse across applied torque levels (Fig. 9), with a mean impulse of 9.92 µN·m·s. In contrast, the control beam exhibited a negative relationship between increasing applied torque and impulse. Control beam impulse decreased from 44.6 µN·m·s at the lowest applied torque to 20.8 µN·m·s at the highest.

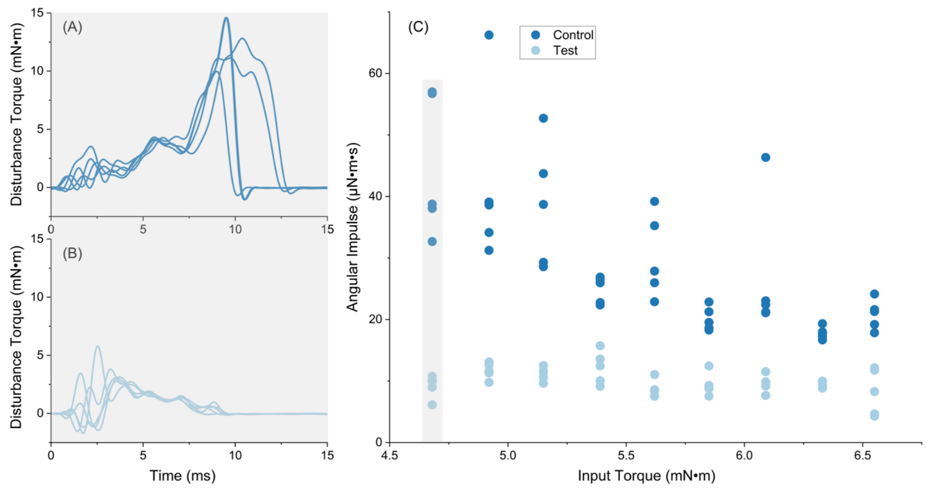

Figure 9: (A and B) Representative time series data for 5 trials of the control beam (A) and the test beam (B) at the lowest torque input setting. (C) Angular impulse measurements for the control (dark blue) and the test (light blue) beams at the 9 different input torque settings.

Peak disturbance torques occur at earlier angular displacements in the test beam than the control beam (Fig. 10). The disturbance torque in the control beam continues to increase throughout the disturbance contact. Integrating the disturbance torque–displacement data allowed us to evaluate angular work (Fig. 10). Average angular work imparted by the disturbance was over 3 times lower in the test beam than the control beam, with a mean of 302.28 µJ and 966.80 µJ respectively. Unlike angular impulse and ISE, angular work was invariant across applied torque levels for both beams.

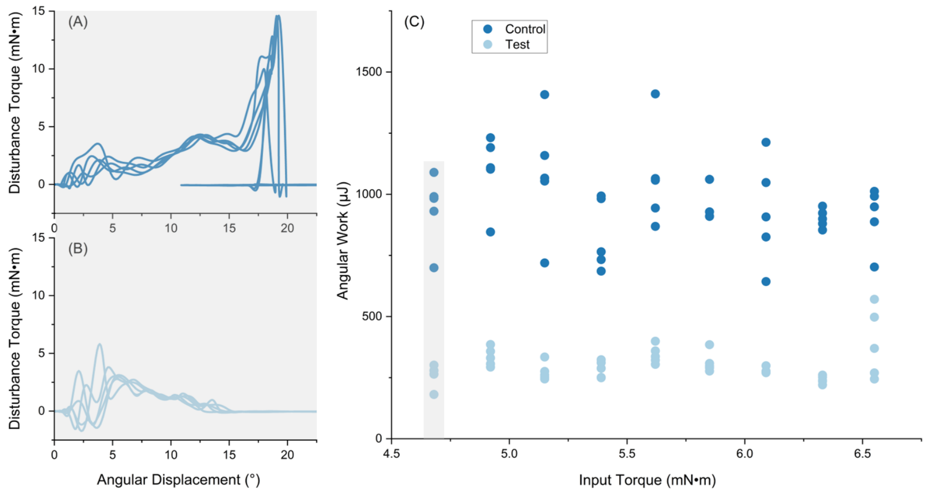

Figure 10: (A and B) Representative torque-angular displacement data for 5 trials of the control beam (A) and the test beam (B) at the lowest torque input setting. (C) Angular work measurements for the control (dark blue) and the test (light blue) beams at the 9 different input torque settings.

Discussion

Insects possess biomechanical adaptations to prevent irreversible damage and reduce destabilization during wing impact events. Though similar bio-inspired buckling joints have been shown to improve stability following collisions in FWMAVs [1, 5], the underlying physics that aids such passive stabilization is not well understood. To address this gap, we designed two structures: a test beam, comprised of two flexible beam segments spanned by a bio-inspired buckling joint, and a homogeneous control beam for comparative analysis to isolate the effects of buckling. Both beams were subjected to a series of quasi-static and dynamic tests. First, we conducted a quasi-static torque–angular displacement test to evaluate the linear stiffness and hysteresis behavior. We then performed a dynamic experiment to evaluate the angular work done and angular impulse imparted by an obstacle as the beam was rotated through it by a motor. We further quantified how the beam trajectory differed between disturbed and undisturbed trials. Here, we comment on our findings and conjecture how both material and geometric effects may contribute to more stable flight.

Buckling Test Beam Exhibits Hysteresis

Torque–angular displacement profiles confirmed that both beams exhibit comparable stiffness in the linear range (Fig. 7). At larger angles (>3°), the behavior in the control and test beams differed, indicating that the observed differences between the beams in our data were due to the nonlinear buckling behavior of the test beam. Beyond the critical buckling angle, the test beam displayed a nonlinear response with significantly reduced torque capacity and about three times the hysteresis area as the control beam.

The torque–angular displacement curves characterize the potential energy storage behavior of the beams. The difference between the loading and unloading curves reflects how much of the input motor work is recoverable compared to what is lost to viscoelasticity or friction. For perfectly elastic materials, stored energy is completely recoverable, characterized by overlapping loading and unloading curves and no hysteresis loop. This case is most similar to our control beam. In viscoelastic materials, some energy is dissipated as heat, and is dependent on both deformation and time [40]. These materials recover their original shape like elastic solids, but their response is rate and duration dependent. The control and test beam segments are made of PLA based print filament known for its high elastic modulus, but low percent elongation and strain energy density [41]. In contrast, the buckling joint is constructed from thermoplastic polyurethane, a rubber-like polymer that exhibits hyperelastic nonlinear behavior and hysteretic properties [42]. Given these material differences, hysteresis area is measurably higher in the buckling test beam than the control beam, 98.4 μJ and 32.3 μJ respectively. This result is both because the majority of deformation is localized to the viscoelastic polyurethane joint, and because the rapid deformation during buckling likely exceeds the deformation rates in the control beam that are dominated by the motor loading rate. The increased deformation rate from buckling would then amplify rate-dependent energy losses in the buckle joint material. In our case, the control beam response is not perfectly elastic and displays measurable hysteresis. While some of this hysteresis may be attributed to internal losses, friction losses from slip at the force cell may contribute to the hysteresis as well.

Although the buckling beam dissipates more energy than the control beam at the tested loading rate, this dissipation is unlikely to explain the reduced angular work and impulse observed in the dynamic disturbance study (see section 2). Nonetheless, buckling may still provide a flight-stabilizing benefit by damping free vibrations that follow a wing strike. Because the vibrations of flexible beam segments were not measured here, future work could investigate whether wing buckling attenuates whole-beam oscillations after collisions.

Test Beam Improved Stability in Dynamic Disturbance Experiments

Trajectories of both beams showed that the buckling joint increases path recovery following a disturbance (Fig. 8). We used ISE to characterize the overall trajectory disruption at different motor input settings (Fig. 8) and found that the control beam averages were 8.8 and 115 times higher than the test beam averages at the lowest and highest input torques, respectively. Additionally, ISE decreased with increasing motor input torque in both beams. This trend is also evident in Fig.8, which shows the kinematic data at the two range extremes.

We can interpret the path disruption as it relates to impulse (Fig. 9) imparted on the system by the disturbance. In these tests, the motor applies a constant torque independent of the opposing disturbance torque from the obstructing force cell. The severity of kinematic change induced by the disturbance is affected by the ratio of the motor impulse to the opposing impulse of the disturbance. When the motor torque is small, the fixed disturbance represents a larger opposing impulse to the total angular momentum of the system, leading to deviations in the trajectory compared to a beam path with no disturbance. We can estimate the impulse from the motor over the same time period used for the ISE paths. For the test beam at the lowest motor torque setting, we found that the motor impulse is 13.09 times larger than the average disturbance impulse, whereas in the control beam the motor impulse is only 2.38 times larger. At the highest motor input, the test beam and control beam have motor to disturbance impulse ratios of 17.42 and 6.516 respectively. This difference in relative impulses provides a mechanistic explanation for the improved path recovery of the test beam, particularly at low input torque.

We can further contextualize the influence of the buckling joint by analyzing the angular work done to the beam during dynamic experiments. The angular work arises from two sources: the motor, which applies a torque at the beam base, and the obstacle, which creates an opposing torque when the beam is in contact. Absent the obstacle, all angular work done by the motor is converted into rotational kinetic energy, assuming frictional losses and beam potential energy storage are negligible. With the obstacle present, a large fraction of motor work is stored as strain energy in the beam until it deforms enough to clear the obstruction. We found that the angular work done by the obstacle was agnostic to input torque (and implicitly, loading rate), for both the control and test beams. Hence, we hypothesize that the energy required to overcome the obstacle was fixed across the loading rates tested for both beam structures. However, considerably less energy is required for the test beam to clear the obstacle compared to the control beam. This is likely because the buckling joint behaves nearly as a hinge, permitting the distal segment of the test beam to rotate without the two flexible beam segments deforming considerably. Thus, buckling is beneficial because it reduces the energetic cost of clearing obstacles by allowing localized hinge-like motion instead of widespread beam deformation.

Implications in Robotics

Our findings suggest that wing buckling may confer several advantages to FWMAVs. First, the presence of the buckling joint lowers angular momentum change, passively reducing the influence of external disturbances and improving trajectory path following. Second, the buckling joint exhibits a consistent impulse response across different input conditions, whereas the control beam varies. This could simplify active control strategies, because the controller would not need to adjust for variable responses, and instead could apply the same counter adjustment regardless of collision input severity. Additionally, the buckling beam may be able to pass through obstacles that the control beam cannot. In these experiments, the lower end of the motor torque range was limited so that both beams could clear the force cell at the lowest setting. At lower motor torques or under larger disturbances, however, it is likely that the test beam could successfully pass through some obstructions that would cause the control beam to stall. In the context of an FWMAV, a wing that can traverse an obstruction without stalling or breaking can resume periodic flapping with minimal disruption, whereas a stall interrupts the wing beat and introduces aerodynamic asymmetries that increase the risk of losing control. Alternatively, a stiff-winged robot may simply be unable to pass through a narrow space that a wing with compliant or buckling mechanisms could negotiate.

To summarize, we demonstrated that a bio-inspired buckling joint may improve disturbance recovery by lowering angular impulse and work imparted by collisions in controlled dynamic tests. The joint's hinging geometry likely localizes strain and limits whole-beam deformation, while its hysteretic behavior may damp post-collision vibrations, further contributing to stability. Together, these results provide a mechanistic understanding of how variable-stiffness joints can passively improve collision robustness in aerial robotic systems.

Acknowledgments

This research was supported by the National Science Foundation under award no. CMMI-1942810 to M.J. and DGE-2439625 to J.M. Any opinions, findings, and conclusions or recommendations expressed in this material are those of the author(s) and do not necessarily reflect the views of the National Science Foundation.

Data Availability

The data and analyses used in this study are freely available at: https://zenodo.org/records/17289526.

CONCLUSION

Concluding Remarks

This work investigates the stabilizing role of a bio-inspired buckling joint through two experimental studies: a quasi-static torque–angular displacement study and a dynamic disturbance study. The results show that the buckling test joint dissipates more energy under quasi-static loading, and in dynamic disturbance trials it reduces impulse, work transfer, and path-following error compared to the control beam. Beyond demonstrating the stability benefits of this buckling mechanism, this study introduces an experimental framework for evaluating other passive joint designs, and provides empirical results that can be used to tune and validate future computational models.

Key Findings

- In the quasi-static experiments, the test beam exhibited an average hysteresis area approximately three times larger than that of the control beam. This indicates that the buckling joint has a time-dependent material response and dissipates substantially more energy than the control. The control beam, however, also displayed measurable hysteresis, likely due in part to frictional losses at the force cell interface. Higher hysteresis in the test beam suggests that this design behaves more like a damper than an elastic spring, dissipating energy instead of storing it for later release.

- In the dynamic disturbance study, the test beam showed over a 90% reduction in average ISE for six of the nine input conditions, with average reductions across input conditions ranging from 78% to more than 99%. These reductions in ISE demonstrate that the buckling joint preserves trajectory fidelity and minimizes the need for motor position correction after a disturbance. Additionally, ISE decreased with increasing input torque in both beams. This trend suggests that the relative influence of a disturbance diminishes as system momentum increases, and that momentum itself provides a degree of passive disturbance robustness, independent of structural compliance.

- The test beam exhibited lower angular impulse and work quantities than the control beam. Average impulse in the test beam was up to 80% lower than in the control beam, and average work was approximately 70% lower across all input conditions. We predicted that the relative intensity of the disturbance impulse would influence the severity of path-following error. To quantify this relationship, we compared the motor impulse to the opposing disturbance impulse across different motor input levels. The results indicated that the buckling joint substantially reduced the effective impulse transmitted by the disturbance, allowing the motor's driving impulse to dominate, thereby improving path recovery especially at higher motor input torques.

- Work did not vary with motor input, indicating a consistent energy requirement to overcome the force cell obstruction across all loading rates for each beam. A large portion of the motor work was likely stored as strain energy as the beams deformed against the obstruction. However, by localizing this deformation to the buckle joint, the test beam required substantially less energy to clear the obstacle than the control beam. In effect, we hypothesize that the buckling joint behaves as a hinge, allowing localized rotation while restricting bending in the surrounding structure, thereby reducing the overall strain energy needed to pass the obstruction.

Supplemental Findings

We found that angular work was invariant to input torque, whereas angular impulse decreased with increasing input torque for the control beam, and not the test beam. Because the disturbance torque is the same for both quantities, the differing trends arise from variations in the domains over which torque is integrated: time for impulse and angular displacement for work. Ideally, contact duration and displacement range would have been quantified directly from the experimental data; however, signal noise made it difficult to precisely identify the start and end of contact. We instead identified contact domains through high-speed video analysis available at: https://zenodo.org/records/17289526. A shorter contact duration at higher input torques would therefore produce a decreasing impulse trend, consistent with what we observed in the control beam. Our supplemental high-speed videos support this interpretation. In the control beam, contact duration with the force cell decreased from 7.5 ms at the lowest motor input to 4.5 ms at the highest, while the test beam showed a smaller relative change, from 5.0 ms to 4.3 ms.

Future Directions

A next step for this research is to develop a complementary computational model. Finite element models of both the control beam and buckling beam should be constructed in Abaqus FEA software with the experimental conditions and joint design studied here. By tuning the models against measured disturbance torques and kinematic trajectories, they can be validated as reliable predictors of system behavior. Once validated, it would serve as a predictive tool for further design exploration and can give us additional information about the system such as stress and strain throughout the length of the beams.

With the validated model, parametric studies should be performed to explore design parameters. For example, modifications in joint placement and hinge geometry (see Tab.1) could be evaluated to understand their effects on the critical buckling angle, or overall torque attenuation. In designing the physical experiment, beam and joint dimensions were chosen with consideration of the motor's capabilities. During preliminary quasi-static tests, the motor operating in position-control mode could not generate sufficient torque to displace the control beam through the full buckling range of the test beam. To address this limitation, beam parameters were specified to favor earlier buckling in the test beam and to reduce overall rigidity in both beams, ensuring that the motor could reliably drive the system through the range of interest. However, later onset of buckling and greater overall rigidity may more closely replicate biological mechanisms [1, 3, 5] and ultimately be more advantageous for flight performance in a robot. Future work could explore these alternative parameters through the computational model for a broader understanding of how different buckling thresholds may influence stability and robustness following collision. Additionally, the scalability of the beam and joint dimensions should be explored within the model. It would be useful to predict how buckling mechanisms behave across different size ranges of FWMAVs wings and inform whether the same principles hold for millimeter-scale devices and larger robotic fliers.

Material selection also remains an important design consideration. From the torque-displacement results we found that this joint displays hysteresis, but some insect buckling joints, like the costal break in yellowjackets, are known to have resilin [2], a protein in many insects and other arthropods with exceptionally high elastic efficiency [43]. Resilin presence in the costal break suggests that elastic storage plays a role in the mechanism's function. Our results indicate that the artificial buckling joint is instead dissipating energy like a damper and may store considerably less elastic energy than a resilin-based structure. However, with a validated finite element model, different constitutive material models could be substituted to predict how elastomers, composites, or bio-inspired hybrid materials influence energy dissipation differently than the polyurethane material used in our joint. This capability would be especially useful for scaling the design to smaller or larger geometry, where material properties may interact differently with geometric compliance.

REFERENCES CITED

[1] Hoang Vu Phan and Hyun Cheol Park. Mechanisms of collision recovery in flying beetles and flapping-wing robots. *Science*, 2020.

[2] Andrew M Mountcastle and Stacey A Combes. Biomechanical strategies for mitigating collision damage in insect wings: structural design versus embedded elastic materials. *Journal of Experimental Biology*, 2014.

[3] Mark Jankauski, Ryan Schwab, Cailin Casey, and Andrew Mountcastle. Insect Wing Buckling Influences Stress and Stability During Collisions. *Journal of Computational and Nonlinear Dynamics*, 2022.

[4] T. G. Bayley, G. P. Sutton, and M. Burrows. A buckling region in locust hindlegs contains resilin and absorbs energy when jumping or kicking goes wrong. *Journal of Experimental Biology*, 215(7):1151–1161, 2012. Accessed: 2025-08-29.

[5] Andrew M Mountcastle, E Farrell Helbling, and Robert J Wood. An insect-inspired collapsible wing hinge dampens collision-induced body rotation rates in a microrobot. *Journal of The Royal Society Interface*, 2019.

[6] Hao Liu, Ravi Sridhar, Dmitry Kolomenskiy, and Hiroto Tanaka. Biomechanics and biomimetics in insect-inspired flight systems. *Philosophical Transactions of the Royal Society B: Biological Sciences*, 371(1704):20150390, 2016.

[7] Mohammad Nasirul Haque, Bo Cheng, Bret W. Tobalske, and Haoxiang Luo. Hummingbirds use wing inertial effects to improve manoeuvrability. *Journal of the Royal Society Interface*, 20(20230229), 2023. Accessed: 2025-08-29.

[8] Robin J. Wootton. The mechanical design of insect wings. *Scientific American*, 263(5):114–121, 1990. Accessed: 2025-08-29.

[9] H. K. Kwon and J. W. Chang. Effects of shapes and kinematics of hovering flapping wings on aerodynamic forces and vortex structures. *Scientific Reports*, 15:5098, 2025. Accessed: 2025-08-29.

[10] Fa Song, Yongwei Yan, and Jiyu Sun. Review of insect-inspired wing micro air vehicle. *Arthropod Structure & Development*, 2023. Epub 2022-Dec-1.

[11] Hoang Vu Phan and Hyun Cheol Park. Insect-inspired, tailless, hover-capable flapping-wing robots: Recent progress, challenges, and future directions. *Progress in Aerospace Sciences*, 2019.

[12] Kevin Y. Ma, Pakpong Chirarattananon, Sawyer B. Fuller, and Robert J. Wood. Controlled flight of a biologically inspired, insect-scale robot. *Science*, 340(6132):603–607, 2013.

[13] Yao-Wei Chin. Efficient flapping wing drone arrests high speed flight using post-stall soaring. *Science Robotics*, 2020.

[14] Matej Karásek, Florian T. Muijres, Christophe De Wagter, Bart D. Remes, and Guido C. H. E. de Croon. A tailless aerial robotic flapper reveals that flies use torque coupling in rapid banked turns. *Science*, 2018.

[15] Hoang Vu Phan and Hyun Cheol Park. Design and evaluation of a deformable wing configuration for economical hovering flight of an insect-like tailless flying robot. *Bioinspiration & Biomimetics*, 2018.

[16] Shengjie Xiao, Yuhong Sun, Dapeng Ren, Kai Hu, Huichao Deng, Yun Wang, and Xilun Ding. Design and flight performance of a bio-inspired hover-capable flapping-wing micro air vehicle with tail wing. *Aerospace*, 10(11), 2023.

[17] Arash Roshanbin, Hamid Altartouri, Matej Karásek, and André Preumont. Colibri: A hovering flapping twin-wing robot. *International Journal of Micro Air Vehicles*, 2017.

[18] Danusha J. Foster and Ralph V. Cartar. What causes wing wear in foraging bumble bees? *Journal of Experimental Biology*, 214(11):1896–1901, 2011. Accessed: 2025-08-29.

[19] Reuven Dukas and Lauren Dukas. Coping with nonrepairable body damage: effects of wing damage on foraging performance in bees. *Animal Behaviour*, 2011.

[20] Ralph V Cartar. Morphological Senescence and Longevity: An Experiment Relating Wing Wear and Life Span in Foraging Wild Bumble Bees. *Journal of Animal Ecology*, 1992.

[21] Claudia Haas and R Cartar. Robust flight performance of bumble bees with artificially induced wing wear. *Canadian Journal of Zoology*, 2008.

[22] S. Ravi, T. Siesenop, O. Bertrand, L. Li, C. Doussot, W. H. Warren, S. A. Combes, and M. Egelhaaf. Bumblebees perceive the spatial layout of their environment in relation to their body size and form to minimize inflight collisions. *Proceedings of the National Academy of Sciences of the United States of America*, 117(49):31494–31499, 2020. Accessed: 2025-08-29.

[23] Julien R. Serres and Franck Ruffier. Optic flow-based collision-free strategies: From insects to robots. *Arthropod Structure & Development*, 46(5):703–717, 2017. From Insects to Robots.

[24] Emily Baird and Marie Dacke. Finding the gap: a brightness-based strategy for guidance in cluttered environments. *Proceedings of the Royal Society B: Biological Sciences*, 283(20152988), 2016. Accessed: 2025-08-29.

[25] Andrew M Mountcastle and Stacey A Combes. Wing flexibility enhances load-lifting capacity in bumblebees. *Proceedings of the Royal Society B: Biological Sciences*, 2013.

[26] Heidi E. Reid, Ryan K. Schwab, Miles Maxcer, Robert K. D. Peterson, Erick L. Johnson, and Mark Jankauski. Wing flexibility reduces the energetic requirements of insect flight. *Bioinspiration & Biomimetics*, 2019.

[27] Hamed Rajabi, Jan-Henning Dirks, and Stanislav N Gorb. Insect wing damage: causes, consequences and compensatory mechanisms. *Journal of Experimental Biology*, 2020.

[28] R. J. Wootton. Support and deformability in insect wings. *Journal of Zoology*, 1981.

[29] Stacey A. Combes and Thomas L. Daniel. Flexural stiffness in insect wings i. scaling and the influence of wing venation. *Journal of Experimental Biology*, 206(17):2979–2987, 2003.

[30] H. Park, G. Bae, and I. Kim. Development of flapping wing robot and vision-based obstacle avoidance strategy. *Journal of Field Robotics*, 40(3):456–470, 2023.

[31] T. Kim, I. Hong, S. Im, et al. Wing-strain-based flight control of flapping-wing drones through reinforcement learning. *Nature Machine Intelligence*, 6:992–1005, 2024.

[32] Zhan Tu, Fei Fei, Jing Zhang, and Xinyan Deng. Acting is seeing: Navigating tight space using flapping wings. In *Proceedings of the IEEE International Conference on Robotics and Automation (ICRA)*, pages 95–101, 2019.

[33] Pooya Sareh, Pisak Chermprayong, Marc Emmanuelli, Haris Nadeem, and Mirko Kovac. Rotorigami: A rotary origami protective system for robotic rotorcraft. *Science Robotics*, 3(22):eaah5228, 2018.

[34] Xiang Lu, Yulie Wu, Jie Chen, Yang Chen, Xuezhong Wu, and Dingbang Xiao. An insect-scale flapping-wing micro aerial vehicle inspired by tumblers capable of uncontrolled self-stabilizing flying. *Research*, 8:Article ID: 0787, 2025.

[35] YuFeng Chen, Siyi Xu, Zhijian Ren, and Pakpong Chirarattananon. Collision resilient insect-scale soft-actuated aerial robots with high agility. *IEEE Transactions on Robotics*, 37(5):1752–1764, 2021.

[36] Yufeng Chen, Hongqiang Wang, E. Farrell Helbling, Noah T. Jafferis, Raphael Zufferey, Aaron Ong, Kevin Ma, Nicholas Gravish, Pakpong Chirarattananon, Mirko Kovac, and Robert J. Wood. A biologically inspired, flapping-wing, hybrid aerial-aquatic microrobot. *Science Robotics*, 2(11):eaao5619, 2017.

[37] Stefano Mintchev, Sebastien De Rivaz, and Dario Floreano. Insect-Inspired Mechanical Resilience for Multicopters. *IEEE Robotics and Automation Letters*, 2017.

[38] Bradley H Dickerson, Zane N Aldworth, and Thomas L Daniel. Control of moth flight posture is mediated by wing mechanosensory feedback. *Journal of Experimental Biology*, 2014.

[39] Myriam J Uhrhan, Richard J Bomphrey, and Huai-Ti Lin. Flow sensing on dragonfly wings. *Annals of the New York Academy of Sciences*, 2024.

[40] Maria Cristina Tanzi, Silvia Farè, and Gabriele Candiani. *Foundations of Biomaterials Engineering*. Academic Press, 2019.

[41] A. Ghaznavi Youvalari, J. Alizadeh Kaklar, and M. Mohamadi. Investigation of mechanical properties in pla, abs and epoxy resin parts fabricated by 3d printing technology. *Scientific Reports*, 2025.

[42] H. J. Qi and M. C. Boyce. Stress–strain behavior of thermoplastic polyurethanes. *Mechanics of Materials*, 2005.

[43] Svend Olav Andersen. Characterization of a New Type of Cross-Linkage in Resilin, a Rubber-Like Protein. *Biochimica et Biophysica Acta*, 1963.